PCCP

Imaging inelastic scattering of CO with Argon: polarization dependent differential cross sections

Journal:	*Physical Chemistry Chemical Physics*
Manuscript ID	CP-ART-02-2019-000876.R1
Article Type:	Paper
Date Submitted by the Author:	02-Apr-2019

Complete List of Authors:	Sun, Zhong-Fa; Radboud University of Nijmegen, IMM Molecular and Laser Physics Bishwakarma, Chandan ; Radboud University of Nijmegen, IMM Molecular and Laser Physics Song, Lei; University of Stuttgart, Institute for Theoretical Chemistry, van der Avoird, Ad; Institute of theoretical chemistry van Hemert, Marc; Universiteit Leiden, Chemistry McBane, George; Grand Valley State University, Chemistry Suits, Arthur; University of Missouri Columbia College of Arts and Science, Chemistry Parker, David; Radboud University of Nijmegen, IMM Molecular and Laser Physics;

Imaging inelastic scattering of CO with Argon: polarization dependent differential cross sections

Zhong-Fa Sun[1], Chandan K. Bishwakarma[1], Lei Song[2], Ad van der Avoird[2], Marc C. van Hemert[3], Arthur G. Suits[4], George C. McBane[5], and David H. Parker[1*]

1. Department of Molecular and Laser Physics, Institute for Molecules and Materials, Radboud University, Heyendaalseweg 135, 6525 AJ Nijmegen, The Netherlands
2. Theoretical Chemistry, Institute for Molecules and Materials, Radboud University, Heyendaalseweg 135, 6525 AJ Nijmegen, The Netherlands
3. Leiden Institute of Chemistry, Gorlaeus Laboratories, Leiden University, Einsteinweg 55, 2333 CC Leiden, The Netherlands.
4. Department of Chemistry, University of Missouri, Columbia MO 65211, USA
5. Department of Chemistry, Grand Valley State University, Allendale, MI 49401, USA

Abstract:

Rotationally inelastic scattering of carbon monoxide (CO) with Argon at a collision energy of 700 cm^{-1} has been investigated by measuring polarization dependent differential scattering cross sections (PDDCSs) for rotationally excited CO molecules using a crossed molecular beam apparatus coupled with velocity-map ion imaging. A simple and robust (1+1'+1") VUV (Vacuum Ultra-Violet) REMPI (Resonance Enhanced Multi Photon Ionization) scheme is used and images are obtained by setting the VUV light polarization direction parallel or perpendicular to the scattering plane. Clear differences between the images for the two polarizations are observed, indicating strong collision induced alignment of the rotational angular momentum of scattered CO. A direct image analysis procedure as described in our previously published paper (A. G. Suits *et al*., *J*. *Phys*. *Chem*. *A* 2015, **119**, 5925), is employed to extract the fully quantum state resolved alignment-free differential cross sections (DCSs) and the state-to-state angle-dependent alignment moments for each final rotational state. The experimental results are compared with advanced theory, in particular with the predictions of CC QM (Close-Coupling Quantum Mechanical) and QCT (Quasi-Classical Trajectory) calculations. The agreement between experiment and theory is generally found to be quite good throughout the entire scattering angle range for all the final states probed, showing the reliability of the experiment and use of the direct extraction method, as well as the accuracy of the potential surface over the studied collision energy range. A classical kinematic apse (hard shell) model was found to be useful in interpreting the measured collision induced alignment moments.

1. Introduction

Rotationally inelastic scattering of small molecules with atoms is an active research field that continues to offer surprising new insights into fundamental aspects of atomic and molecular interactions.[1-8] While numerous experimental investigations have reported state-to-state cross sections of vibrational and rotational energy transfer, investigations that experimentally measure collision induced angular momentum polarization (usually referred to as collision induced alignment or CIA) are less common. CIA should always arise in such scattering processes, but can be difficult to quantify experimentally. Information derived by detection of collision induced angular momentum polarization in a crossed beam scattering experiment provides a more complete test for quantum scattering calculations. The group of Meyer reported early

investigations of CIA of NH_3 molecules in a counter-propagating beam scattering experiment utilizing resonance enhanced multiphoton ionization (REMPI)-time of flight (TOF) spectra.[9, 10] Velocity map imaging[11] allows a more convenient and direct detection of collision induced polarization in inelastic scattering because of its ability to probe the full polarization dependent differential cross section (PDDCSs) in one measurement.[12, 13] The groups of Chandler and Cline have used a (1+1') REMPI ionization scheme and velocity map imaging to study collision induced alignment of NO with argon[14, 15] and even determined the angle-dependent orientation of the product molecule rotation in the collision plane.[16] Later, collision induced orientation and alignment effects in the rotational angular momentum of NO after colliding with rare gas atoms as a function of the scattering angle were reported by Brouard and coworkers, who used hexapole selection for the initial NO state preparation.[17-21] So far, rotational alignment of the NO molecule due to inelastic scattering with an Ar atom has been studied most extensively, whereas there have been fewer studies on collision induced polarization effects for other systems.

This paper describes an experimental study of CIA for inelastic scattering of carbon monoxide, CO, with Ar at a mean collision energy of 700 cm^{-1}. A closed-shell molecule such as CO is attractive for probing alignment effects compared to the open-shell NO molecule, which shows alignment depolarization due to slow angular momentum coupling with electron spin. However, detection of CO using velocity map imaging is much more challenging than detection of NO because the excited electronic states of CO that can be used as resonance step in the ionization lie deep in the vacuum ultraviolet (VUV). Here, we employ a simple three-color VUV REMPI detection scheme where all three colors come from the difference frequency mixing process used for VUV generation, and the VUV radiation is not separated from the two incident laser beams needed for its generation. Ref. 22 characterized this VUV detection method as a (1+1'+1") REMPI process[22] which can be combined with velocity map imaging to measure polarization dependent differential cross sections (PDDCSs). Another recent study[23] from our group reported CO+He scattering PDDCSs using this VUV detection scheme, together with regular DCSs measured using polarization insensitive 2+1 REMPI of CO via its $E^1\Pi$ state. A simple analysis scheme for extracting collision induced alignment moments directly from the polarization sensitive images measured with velocity map imaging was established by Suits *et al.* as described in ref. 24. By contrast, the Brouard group uses (with success) a basis set expansion approach that reproduces the experimental images in order to obtain the alignment parameters.[19, 21]

In an earlier paper we tested the direct extraction analysis method for CO collisions with Ar producing CO (j' = 9) and found very good agreement of the predictions from advanced *ab-initio* theory with the experimental PDDCSs.[24] In these experiments, a 3-dimensional Newton sphere of scattered CO molecules is formed and crushed onto a 2-dimensional imaging detector to form a 2-dimensional Newton disk. Pairs of the CO+Ar scattering images collected with vertical and horizontal polarization of the detection laser provides information on both the polarization

independent DCS and two alignment moments[25] $A_0^{\{2\}}$ and $A_{2+}^{\{2\}}$ that characterize the rotational angular momentum distributions. (In contrast to the previous study of CO+He scattering,[23] the experimental geometry used for CO+Ar scattering[24] is insensitive to the $A_{1+}^{\{2\}}$ moment.) We show in the present paper that the direct analysis yields DCSs, $A_0^{\{2\}}$ and $A_{2+}^{\{2\}}$ parameters that agree well with predictions by different high-level theoretical calculations for the full range of accessible CO *j'* final states from CO+Ar scattering.

2 Methods

2.1 Experiment

The crossed-beam experiment combines velocity map imaging (VMI)[11] and a state selective VUV REMPI scheme[22] to allow polarization sensitive detection. The apparatus has been described in detail elsewhere,[24] so only a brief description is given here. Figure 1 presents an overall view of the experimental setup which consists of a rotatable crossed molecular-beam machine coupled with VMI ion optics and the laser systems for VUV generation. Two skimmed supersonic beams were crossed at a collision angle of 90° at the center of the VMI ion optics in the scattering chamber; one was a neat pure argon beam produced using a Nijmegen pulsed valve (NPV)[26] and the other beam, generated from a Jordan pulsed valve (JPV), contained 5% CO seeded in argon. Backing pressure for the supersonic expansion was 1 bar for both colliding beams, and the pulse duration of Nijmegen pulsed valve beam is about 50 µs while the pulse duration of the Jordan valve beam is about 60 µs. A differentially pumped source chamber houses the primary beam (CO) and the molecular beam passed through a skimmer of aperture diameter 2.5 mm positioned 7 cm away from the nozzle. The secondary source (neat Ar) was mounted in the differentially pumped rotatable chamber and positioned 3 cm from the secondary skimmer of aperture diameter 2.5 mm. All three chambers were pumped with separate turbo pumps. Both molecular beams and the VUV laser beam were coplanar. The collision energy, 700 ± 50 cm^{-1}, was determined from the velocity mapped beam spot positions and the spread of two beams (For the secondary beam velocity determination a tiny amount of CO was seeded in the pure Ar beam). This value for the collision energy was confirmed by the variation in radius of the scattering image as a function of the rotationally excited CO internal energy after scattering.

VUV radiation is produced by four wave difference frequency mixing (FWDM) of two dye laser beams in pure xenon gas,[27] as described in detail in ref. 24. One UV dye laser (ω_1) was fixed at 249.618 nm (vac.) for the two-photon resonance transition $5p^6\,{}^1S_0$ - $5p^5 6p\,[\frac{1}{2}]^0$ of Xe and combined with tunable visible radiation around 650 nm (ω_2) from the other dye laser (ω_2) to generate tunable VUV (ω_{VUV}) radiation around 155 nm, where $\omega_{VUV} = 2\omega_1 - \omega_2$. The two incident beams were combined on a 248 nm dichroic mirror and subsequently focused at the same point inside the Xe cell by a combined configuration of plano-convex lenses. A pressure of 30 mbar Xe in the cell was found to result in the optimum VUV production efficiency. Collision induced alignment

of scattered products was probed using different polarizations of the VUV light, which was controlled by rotating the polarization of the visible laser beam. The purity and direction of polarization of the VUV light at the detection zone was confirmed from photodissociation images of OCS.[28]

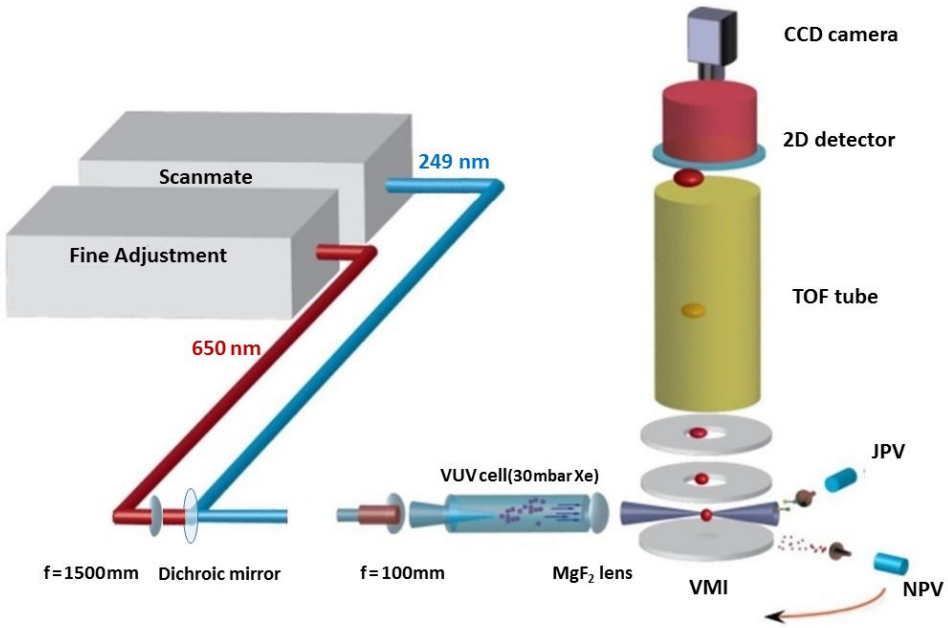

Figure 1: Schematic of crossed-beam VMI experimental setup for (1+1'+1") VUV REMPI detection of aligned CO scattered from Ar. Two perpendicular skimmed supersonic molecular beams were used, one of neat pure argon produced from a NPV and the other of 5% CO/Ar produced from a JPV. The collision angle between the two molecular beams can be changed by rotating one beam about the scattering center in the collision plane. The scattered product is ionized by a VUV REMPI scheme where the VUV radiation wavelength is resonant with a CO $X \rightarrow A$ transition. VUV is generated from four-wave difference frequency mixing in a Xe cell using 249 and 650 nm radiation from two tunable dye laser systems. The VUV polarization is set in or perpendicular to the collision plane by rotating the 650 nm laser polarization. The nascent CO^+ image is projected by VMI ion optics and mass selected by time-of-flight onto a 2D imaging detector and finally recorded by a CCD camera.

The VUV light is tuned into resonance with rotational lines of the CO $A^1\Pi \leftarrow X^1\Sigma^+(j', v = 0)$ transition. Our previous study[22] showed that the next photon step is near-resonance excitation from the $A^1\Pi$ state by the UV light (ω_1) to the $E^1\Pi(v = 6)$ state, followed by ionization by the visible laser (ω_2) beam. Accidental resonance in the second step (ω_1 excitation) leads to enhancement of transitions involving the $j' = 11$ state, which is not probed in this study. The initial state distribution of the CO beam before scattering was optimized from the VUV (1+1'+1") REMPI spectrum of the parent molecular beam signal using the PGOPHER[29] simulation program. Less than 5% out-scattering from the initial state was observed when the Ar beam was present. Figure 2 shows a portion of the VUV (1+1'+1") REMPI spectrum taken for CO after scattering with Ar. We chose the strong Q-branch transitions that are free of overlap with P-branches. Q(13) was not probed, for example, because of overlap with P(8). In the case of Q(7), the laser was set

at the blue shoulder of the transition to avoid overlap with P(7). Separate scattering images for selected Q(*j*') transitions were obtained independently with horizontal (H) and vertical (V) polarization of the VUV radiation, which corresponds to VUV polarization directed in and perpendicular to the molecular beam plane, respectively.

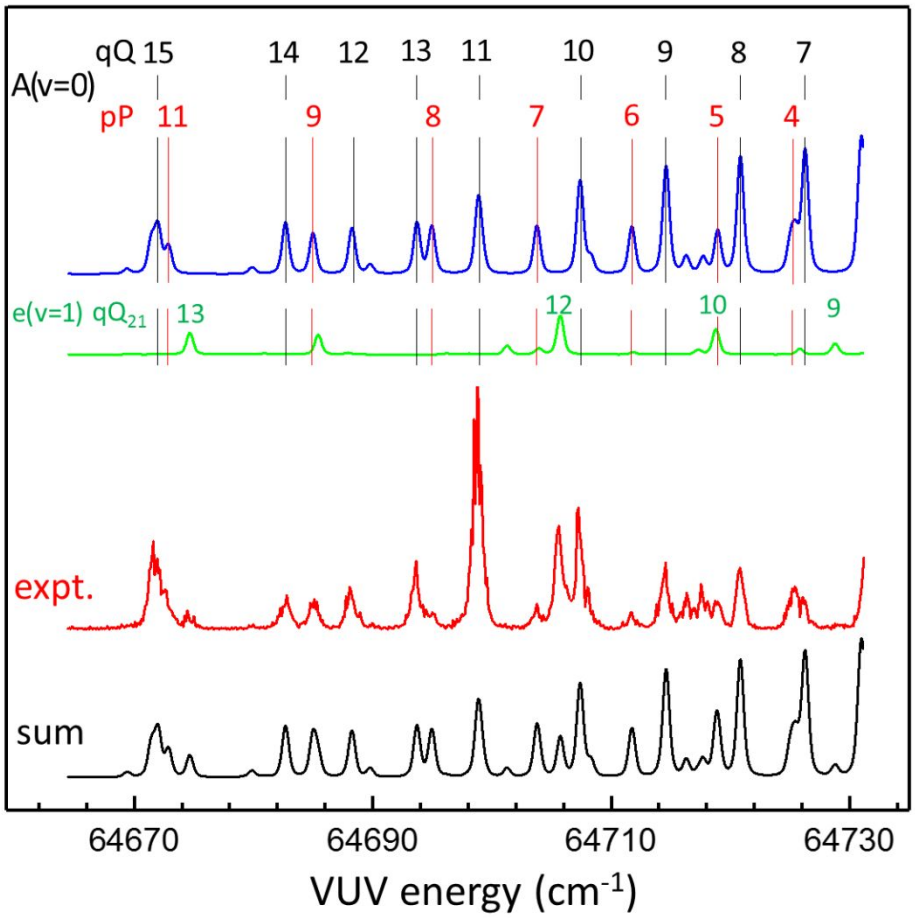

Figure 2 Simulated (PGOPHER)[29] CO $A^1\Pi$ (v = 0) ← $X^1\Sigma^+$(v = 0) VUV spectrum and experimental spectrum obtained while scattering with Ar. The position of the Q(*j*') and P(*j*') branches for the $A^1\Pi$ (v = 0) state simulation (blue line) are labeled in the top row with black label and red label respectively. The second trace shows a simulation of the perturbing $e^3\Sigma^-$(v = 1) state (green line) and the sum of both simulations (black line) is shown in the lowest trace. Above the sum spectrum is the experimental spectrum of scattered CO (red line). The lower two spectra compare favorably and show the enhancement of the Q(11) transition along with the partial overlap of Q(10) with Q_{21}(12) of the *e*-state. A temperature of 300 K was used in the simulation only to make most of the peaks visible; a non-Boltzmann final *j*' state distribution for the experiment is expected.

2.2 Data analysis

Vector correlations provide valuable insight into the molecule-atom scattering process. The relationship between the initial relative velocity vector **k** and final relative velocity vector **k**' of the colliding system gives information about conventional DCSs, whereas the triple-vector correlation between **k**, **k**' and **j**' (scattered product rotational angular momentum) reveals the degree of rotational polarization due to collision; these vector correlations are generally

described in terms of renormalized PDDCSs. Brouard *et al.*[30] have summarized the relationships between the different expressions for polarization moments and alignment parameters used in various literature. The PDDCSs results in this paper are presented in the Hertel-Stoll renormalized convention as $A_q^{\{k\}}(\theta)$. $A_0^{\{0\}}(\theta)$ represents the **k**-**k'** correlation, *i.e.*, the conventional DCS, or so-called alignment-free DCS in the current case, while $A_0^{\{2\}}(\theta)$ and $A_{2+}^{\{2\}}(\theta)$ describe the **k**-**k'**-**j'** triple correlation, which is basically the rotational angular momentum polarization. $A_0^{\{2\}}(\theta)$ describes the alignment distribution of **j'** with respect to **k**, with limiting values of +2, corresponding to $\mathbf{j'} \| \mathbf{k}$ and -1 corresponding to $\mathbf{j'} \perp \mathbf{k}$. $A_{2+}^{\{2\}}(\theta)$ reflects the alignment preference of **j'** along the x axis or y axis of the scattering frame, which are both perpendicular to **k;** x lies in the plane containing **k** and **k'** and y is perpendicular to that plane. $A_{2+}^{\{2\}}(\theta)$ has limiting values of +1 corresponding to **j'** aligned along the x axis and -1 corresponding to **j'** aligned along the y axis.

The experimentally acquired polarization-sensitive images were analyzed as described in detail in a previous publication[24] and only a brief overview will be presented here. Relying on the fact that the angular distribution for out-of-plane scattering is encoded in the distribution along the relative velocity vector in the crushed image, two types of angular distribution components (in-plane component; out-of-plane component) were extracted from H and V polarization images by integrating over an annulus covering the 2-D Newton ring and over a narrow stripe through the middle of the image along the relative velocity vector. In total, four sets of angular distribution components were obtained for each final rotationally excited state *j'*: HIP (horizontal, in-plane), HOOP (horizontal, out-of-plane), VIP (vertical, in-plane) and VOOP (vertical, out-of-plane).[24] On the basis of the fact that the overall detection probability function *P* depends on angular momentum alignment $A_q^{\{k\}}$ and probe sensitivity $F_q^{\{k\}}$ determined by the actual experimental geometry of probe laser polarization, algebraic combination of the four sets of components yield the state-to-state alignment-free DCSs and alignment moments $A_0^{\{2\}}$ and $A_{2+}^{\{2\}}$.

2.3 Image simulation

Full simulations of the experimental polarization-sensitive images are performed using a new-version of the 'Imsim'[31] program, which was recently modified to incorporate the effect of rotational angular momentum polarization.

The image intensity, *I*, arising from molecules scattered with the polar angle θ and detected using our VUV (1+1'+1") REMPI scheme can be written as a product of the state-to-state DCS and a polarization-dependent detection probability:

$$I(\theta) = \frac{d\sigma}{d\theta}(\theta)\, P(\theta;\beta,\alpha,\gamma) \quad (1)$$

$$P(\theta;\beta,\alpha,\gamma) = 1 + h^{(2)}\left[A_0^{\{2\}}(\theta)F_0^{\{2\}}(\beta,\alpha,\gamma) + A_{1+}^{\{2\}}(\theta)F_{1+}^{\{2\}}(\beta,\alpha,\gamma) + A_{2+}^{\{2\}}(\theta)F_{2+}^{\{2\}}(\beta,\alpha,\gamma)\right] \quad (2)$$

where $h^{(2)}$ is the second-rank polarization sensitivity factor for one-photon probing, $A_q^{\{2\}}(\theta)$ are the scattering angle-dependent alignment moments, $F_q^{\{2\}}$ are the geometric factors that describe the dependence of the intensity on the linear probe laser polarization characterized by the angles (β,α,γ): β and α are the polar and azimuthal angles of the probe laser propagation direction in the collision frame, and γ specifies the laser polarization (V or H). Note that angular variables are represented by different symbols in this paper compared to those used in ref. 24 in order to avoid confusion later in the text with symbols used in the quantum and classical trajectory theory sections.

The computation performed by the Imsim simulation program is described by equation (3) of Lorenz *et al*.[4] The program estimates the intensity in a single pixel with a numerical integration over the collision volume, the time before the probe laser fires, the pixel area, and the molecular beam speed distributions. The integrand is the product of a Jacobian factor describing the surface area of the Newton sphere projected onto a single pixel, the ionization probability, the differential cross section, and the molecular beam intensities. Earlier versions of the program included no variation of the ionization probability with product angular momentum alignment for one-photon probe excitation. For the present work the ionization probability function was modified to incorporate equation (2) above in the form presented by Brouard *et al.*,[21] and the geometric description of the experiment was refined to permit an unambiguous determination of the Euler angles β, α, and γ.

In the new "Imsim"[31] program, the "apparatus function" was first simulated with an assumed isotropic DCS based upon all the experimental parameters, such as geometry and spatial conditions of incident molecular beams and laser beam, temporal and velocity distribution of molecular beams, delay between the collision overlaps and laser firing, the kinematic conditions of collisions, and so on. Then theoretically (CC QM) predicted state-to-state alignment-free DCS and alignment moments were input into "Imsim"[31] to evaluate the overall pixel intensity function for simulation, and the experimental polarization-sensitive images were finally simulated based on the overall pixel intensity function.

In order to check the quality and the reliability of polarization-dependent image simulation with the new "Imsim"[31] program, the same direct extraction method that was used to analyze the experimental images was applied to the purely-simulated polarization-dependent images and the results were compared with the theoretical DCSs and alignment moments used in the input file for simulation. In Figure 3, the left panel shows the direct extraction analysis on purely-simulated CO Q(9) images for H and V probe polarizations from the Imsim and the red annulus and rectangle indicate the selected integration regions for in-plane and out-of-plane components extraction, respectively. The same settings for integrating regions as used in analysis of experimental images were applied to the simulated images and the extracted HIP, HOOP, VIP,

VOOP distribution components are shown on the right. The alignment-free DCS and alignment moments were then obtained by algebraic combination of these components in the same way as in the analysis of the experimental images and are shown in Figure 4 in comparison with the theoretical data used as input for the simulation. The extraction analysis on purely-simulated images reproduces the input theoretical curves well, especially in shape, even though some detailed features are not regenerated clearly (such as the second and third rainbows in the DCS, and fine structures in the alignment moments). These tests above have demonstrated the reliability of the new "Imsim" program and the good quality of the polarization-dependent image simulations obtained from it.

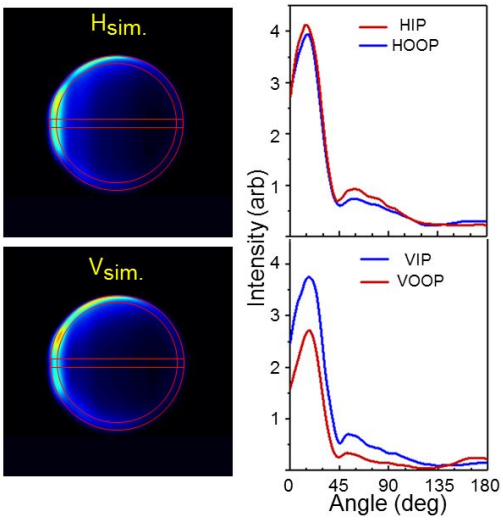

Figure 3: Direct extraction analysis on purely-simulated CO Q(9) images with Imsim program for H and V probe polarizations and the HIP, HOOP, VIP, VOOP distribution components extracted from them. The red annulus and rectangle indicate the selected integration regions for in-plane and out-of-plane components extraction, respectively.

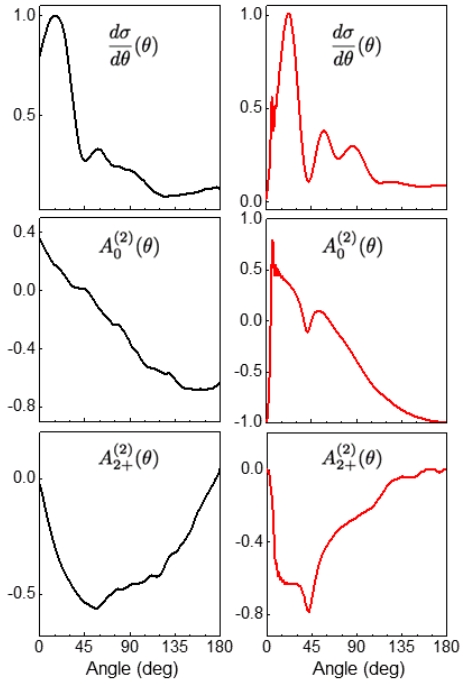

Figure 4: Alignment-free DCS and alignment moments obtained from the analysis of purely-simulated polarization-dependent images (left) and from theory that used as input for simulation

2.4 Theoretical method

Close-coupling quantum mechanical calculations

We used the close-coupling method[32] to compute the differential state-to-state cross sections for CO−Ar collisions as well as the alignment moments of CO due to collision. The CO−Ar potential used in these calculations was obtained from *ab initio* electronic structure calculations with the coupled cluster method by Pedersen *et al*. [32]. We refer to this reference for details of the calculations and the analytic form of the potential. They calculated a three-dimensional (3D) CO−Ar potential which depends on the two intermolecular Jacobi coordinates, as well as on the CO bond length *r*. We used the 2D potential also given in ref. 32 that was obtained by averaging the 3D potential over the ground vibrational (v = 0) state of CO. The close-coupling equations were solved with the renormalized Numerov propagator, with the distance *R* between the Ar atom and the center of mass of CO ranging from 4 to 40 a_0 in 900 steps of equal size. All rotational states of CO up to j = 25 were included in the channel basis and all partial wave contributions up to a total angular momentum of J = 200 were taken into account. The experimental collision energy was estimated to be 700 cm^{-1}, but there is a certain spread in this energy. Hence, the calculations were performed for three different collision energies, 650, 700, and 750 cm^{-1} and the cross sections were averaged with weights of 25, 50, and 25%, respectively. The state-to-state cross sections and CO alignment moments (discussed below) were computed for initial CO states with j = 0 and j = 1 and for all final j' states open at the given collision energies. Our measurements showed that the incoming CO beam contained 80% of j = 0 and 20% of j = 1, so we averaged the calculated results over the initial j = 0 and j = 1 states of CO with these percentages.

The alignment moments $A_0^{\{2\}}(\theta)$ and $A_{\pm}^{\{2\}}(\theta)$ are the irreducible components of the scattering density matrix.[30] The moment $A_0^{\{2\}}(\theta)$ contains the diagonal elements of this density matrix which represent the populations in the different magnetic quantum levels. The off-diagonal elements appearing in the $A_{\pm}^{\{2\}}(\theta)$ moment reveal information about the coherences existing between different eigenstates, which are essential for describing the azimuthal polarization.[25] The scattering angle dependent density matrix is expressed in the scattering amplitudes related to the S-matrix. The QM CC calculations use a basis in which the angular momentum j of the CO monomer is coupled with the angular momentum L of the partial waves describing the relative motion of CO and Ar to a total angular momentum J. This total angular momentum is a conserved quantum number, so that the calculations can be performed separately for each J. The expressions for the DCSs and PDDCSs contain scattering amplitudes in terms of an uncoupled basis and, hence, the S-matrix in terms of the coupled basis had to be transformed to this uncoupled basis before we could obtain the required scattering amplitudes.[33, 34] This uncoupling transformation is needed to resolve the different magnetic (m_j) sublevels of the j states, as well as the scattering angle dependence of the DCSs and alignment moments.

Quasi-classical trajectory calculations

We have here chosen for a full 3D approach because in classical calculations the CO molecule can

acquire sufficient additional energy to have its bond length varying in the range from 2 to 2.25 a_0 already at the collision energy of 700 cm^{-1}. Contrary to the quantum calculations the extra degree of freedom, r_{CO}, causes only 50% extra computer time (calculating the forces is the time determining step). We solved the zero-point-energy leakage problem by using filtering according to the rules advocated by Varandas [35] and others.

We recalculated the CO−Ar intermolecular potential surface for the quasi-classical trajectory calculations, since we found that the potential energy data from ref. 32, calculated primarily for the analysis of the spectroscopy of the CO-Ar van der Waals complex, did not extend to sufficiently short CO-Ar distances. A Jacobi grid consisting of 31 *R* values in the range from 2.6 to 15.0 a_0 and 15 Jacobi angles θ, chosen for optimal quadrature, was applied in coupled cluster singles and doubles with perturbative triples [CCSD(T)] calculations with an augmented quadruple zeta (AVQZ) basis. Midbond functions were not included in the basis since they are considered less relevant for the description of the repulsive part of the potential in collision processes. All calculations were performed with the Molpro 2012 program.[36] Three bond lengths of CO were included: r_e, 0.9 r_e, and 1.1 r_e, where r_e = 1.128 Å is the equilibrium bond length. Interaction energies were derived with the standard counterpoise correction. At each of the *R* and *r* values the angular dependence was represented by an expansion in normalized Legendre polynomials $P_L(\cos\ )$:

$$V(R,r,\Theta) = \sum_L C_L(R,r) \cdot P_L(\cos\Theta) \quad (3)$$

The expansion coefficients $C_L(R,r)$ were obtained from

$$C_L(R,r) = \int P_L(\cos\Theta) V(R,r,\Theta)\, d\cos\Theta = \sum_i w_i \cdot P_L(\cos\Theta_i) \cdot V(R,r,\Theta_i) \quad (4)$$

I.e. the integral over cos Θ is replaced by a weighted sum over cos Θ_i values. The weights and cosine values are dictated by Gauss-Legendre quadrature.

It turned out that *L* values higher than 10 were not needed to obtain good accuracy for energies up to 1.5 times the collision energy E_{coll}: in the attractive part of the potential the standard deviation of the fit was smaller than 0.005 cm^{-1} and in the most repulsive part the standard deviation was still smaller than 0.1 cm^{-1}. The dependence of the expansion coefficients on *R* was fitted with cubic splines under the condition of appropriate asymptotic behavior (exponential increase at short *R*, proper power of R^{-1} at long range). It was found that at each given *R* value the coefficients $C_L(R,r)$ vary linearly with *r* for the *r* values considered. A comparison was made between the potential of the new fit and the one from ref. 32 and it was found that the root mean square difference between the two potentials, determined for 319 geometries with *R* values between 3 and 8 Å was less than 1%.

In all trajectory calculations the Venus code version 2005[37] was used. The program was interfaced with a routine that enables the use of our representation of the interaction energies. The representation of the potential as a Legendre expansion is optimal for quantum methods using a grid of Jacobi coordinates. The Venus program requires the potential as function of (redundant) Cartesian coordinates. The analytic form of the Jacobian matrix needed to also transform the potential derivatives with respect to Jacobi coordinates to derivatives with respect to Cartesian coordinates is more complicated. We therefore chose to apply numerical differentiation where for each Cartesian coordinate a left and right stepsize of 10^{-4} a_0 was used. The CO−Ar intermolecular potential was supplemented with a CO monomer potential, which depends on the bond length r and was represented by a Morse potential. The Morse parameters D_e and r_e were taken from experiment[38] with D_e = 11.24 eV and r_e = 1.128 Å; the parameter in the exponent was adapted to optimally reproduce the set of rovibrational levels in the range spanned by the collision energy. Propagation in time of the Newtonian equations of motion was performed with the Velocity Verlet algorithm with a stepsize of 2×10^{-17} s. Initially the collision partners were set apart with a center of mass distance of 8 Å. A trajectory was considered finished when the center of mass distance had again reached a value of 8 Å. Calculations were performed at a mean collision energy of 700 cm^{-1}. For convenience in the later calculation of differential cross sections and alignment parameters the impact parameters were controlled manually rather than by a random number generator. The maximum impact parameter values b_{max} were found by trial and error and set to 6 Å corresponding to a total angular momentum value for the collision complex of 157. The impact parameter range was stepped from 0 to b_{max} with 0.1 Å steps. At each impact parameter 40000 trajectories, varying in vibrational coordinate and orientation of CO, were generated with the initial values of the rovibrational quantum numbers of CO set to v = 0, j = 0 and v = 0, j = 1. From the Cartesian coordinates and momenta of the atoms at the end of each trajectory the scattering angle and angular momentum vector(s) were determined. Results were binned in the scattering angle (in 40 equally spaced cosine intervals) and j' value (derived from $E_{rot} = j'(j'+1)/2\mu r^2$). This binning provided both the j' dependent partial and differential cross sections. In order to find the scattering angle dependent alignment moments, the angular momentum vectors were transformed to the **k**-**k'** (collision) coordinate system with its z-axis along **k** and x-axis in the **k**-**k'** plane. The alignment moments $A_0^{\{2\}}(\theta)$ and $A_{2+}^{\{2\}}(\theta)$ were calculated based on the formulas described in Table Ⅰ of ref. 12. In each cosine interval of the scattering angle, the alignment moments were determined by the averages:

$$A_0^2 = \langle 3\cos^2\theta - 1 \rangle,$$

$$A_{1+}^2 = \sqrt{3}\langle \cos\theta \sin\theta \cos\varphi \rangle,$$

$$A_{2+}^{2} = \langle \sin^2\theta \cos(2\varphi) \rangle. \quad (5)$$

Here θ is the angle that the angular momentum vector *j*' makes with the z axis, and φ is the angle between the projection of the angular momentum vector in the collision xy plane and the (collision) x axis. The calculated state-to-state cross sections and alignment moments results were averaged over the initial *j* = 0 and *j* = 1 states of CO as described for the close-coupling quantum mechanical calculations.

Since in quasi-classical trajectory methods there is no conservation of vibrational zero-point energy we applied a filter on the outcome of the calculations: only trajectories having a vibrational energy change less than 5% were selected for further analysis. It turned out that lowering this criterion changed the outcome of the analysis only beyond statistical noise (with this setting 99% of the trajectories passed the selection process).

Kinematic Apse model calculation for alignment moments prediction

Calculations of the scattering angle dependent alignment moments have also been carried out based on the kinematic apse (KA) model as described by Khare *et al*.[39] This model considers a simple picture of a classical impulsive collision between an atom and a rigid rotor as that on a hard shell potential. Here the "kinematic apse" vector, defined by (**k**-**k**)/|k'-k| where **k** and **k'** are the initial and final relative velocities, represents the direction of linear momentum transfer. In such a sudden collision, where the molecular axis remains unchanged during interaction, the rotational angular momentum transferred to the diatomic molecule must be perpendicular to the "kinematic apse", *i.e.* the projection of the initial and final rotational angular momenta **j** and **j'** onto the KA are equal; this conservation forms the basis of the KA model. The alignment moments arising from the calculations based on the KA model do not depend on the shape of the hard shell potential, but entirely on the kinematics of the collision. Calculations for the experimentally given mean collision energy were averaged over the experimental collision energy distribution in the same manner as for the CC QM calculations.

3 Results & Discussion

Raw CO^+ images obtained via the Q branch using vertical and horizontal probe laser polarization are presented on the left of Figure 5 for the final states of CO with *j*' = 5, 7, 8, 9, 10, 12, 14. A Newton diagram describing the corresponding experimental geometry is overlaid on the V-polarization image for the product final state *j*' = 5 on the left-top corner. Red arrows in the Newton diagram indicate the velocity vectors of the colliders $\mathbf{v}_{CO}$ and $\mathbf{v}_{Ar}$, the center of mass

velocity $\mathbf{v}_{CM}$, and the initial relative velocity vector **k**. The VUV probe laser beam propagation direction $\mathbf{k}_p$ is also shown. Under the condition that $\mathbf{v}_{CO}$ and $\mathbf{v}_{Ar}$ cross each other at a collision angle of 90°, the average angle between $\mathbf{k}_p$ and **k** is 87°. By consequence the experimental detection sensitivity to the $A_1^{\{2\}}(\theta)$ is low, so this moment was excluded from the image analysis and not presented or further discussed here. The simulated polarization dependent images using CC QM predictions as input for each final state are shown in the middle column of figure 5. The simulated images reproduce the experimental images very well, giving confidence in the ability of the theoretical models to capture the observed stereodynamic features and the validity of the experimental description and kinematic treatment used in the simulations. A tilted small stripe-shaped area of intensity can be seen on the left part of the experimental images, outside of the scattering rings in the forward direction, coinciding with the lab-frame velocity of the un-scattered CO molecular beam, thus called the 'beamspot'. For the majority of *j*' states, the beamspot and the scattered ion signal are well separated in the experimental images; the space between beamspot and scattered ring becomes larger for increasingly higher *j*' states. On the whole, several features of the scattering kinematics and dynamics are immediately apparent from the inspection of the experimental images. The radii of the scattering rings decrease as *j*' increases since the fraction of collision energy required for rotational excitation increases so the fraction partitioned into center-of-mass translational energy decreases. Also noticeable in the experimental images is that the upper (slow) side of the scattering ring in each image looks sharper than the lower (fast) side; this subtle difference arises from kinematic blurring caused by the incident molecular beam velocity spread, which affects the two sideway parts of the scattering ring differently. Finally, a general trend from forward scattering towards sideways and even backward scattering is seen as *j*' increases, which is commonly observed in inelastic scattering studies. Careful inspection of the V and H experimental images reveals clear differences in the forward scattered region and the V experimental images show more sideways and back scattered signal. These are clearly observable effects of collision induced rotational alignment effects in CO+Ar inelastic scattering.

Angular distributions are shown in the right column of Figure 5 with blue and red lines in the graph showing in-plane and out-of-plane components, respectively, as extracted from the flux-corrected H polarization experimental images. Black and green lines show the in-plane and out-of-plane angular distribution components obtained from the V polarization experimental images respectively. As explained in detail in ref. 24, the HIP and HOOP distribution components should be identical due to the equivalence of one specific collision-frame geometry and one specific lab-frame geometry rotated by 90°; and indeed, the blue and red curves overlap each other well. The reliability of the extracted data is affected by numerous factors, including overlap of other transitions with the selected Q(*j*') REMPI transition. For instance, the Q(10) transition is partially overlapped by the $qQ_{21}(12)$ branch of the perturbative $e^3\Sigma^-$ state as shown in Figure 2. In this

analysis we have also assumed that the probe laser propagation direction is perpendicular to the initial relative velocity vector; deviation from this, due especially to the rather large beam angular spreads used in the apparatus, will impact the observed alignment effects. The high probability of elastic scattering, especially in the forward scattered region, and other secondary collision effects can also affect the determination of collision induced alignment due to the inelastic scattering. As shown in Figure 5, the black and green curves become higher as compared to the blue and red curves at larger scattering angles for higher j' states; in addition, a more striking difference between black and green curves in the graph is observed and as *j*' increases this difference increases. These facts imply a larger degree of rotational angular momentum alignment due to collision for the higher final *j*' states, which is also rationalized in the kinematic apse picture from Brouard's group.[30] Brouard *et al.* have shown that rotational alignment in rotationally inelastic scattering of NO with Ar (and in general) originates primarily from the hard shell nature of the interaction potential. Collisions producing higher *j*' states occur at smaller impact parameter and are increasingly sensitive to shorter intermolecular distances and thus the hard shell. For the CO+Ar system, collisional depolarization due to elastic or possibly multiple scattering effects appears to mainly affect the forward scattering regions. By contrast, the backward scattering region shows the maximum possible amount of collision induced alignment, which is visually evident in Figure 5.

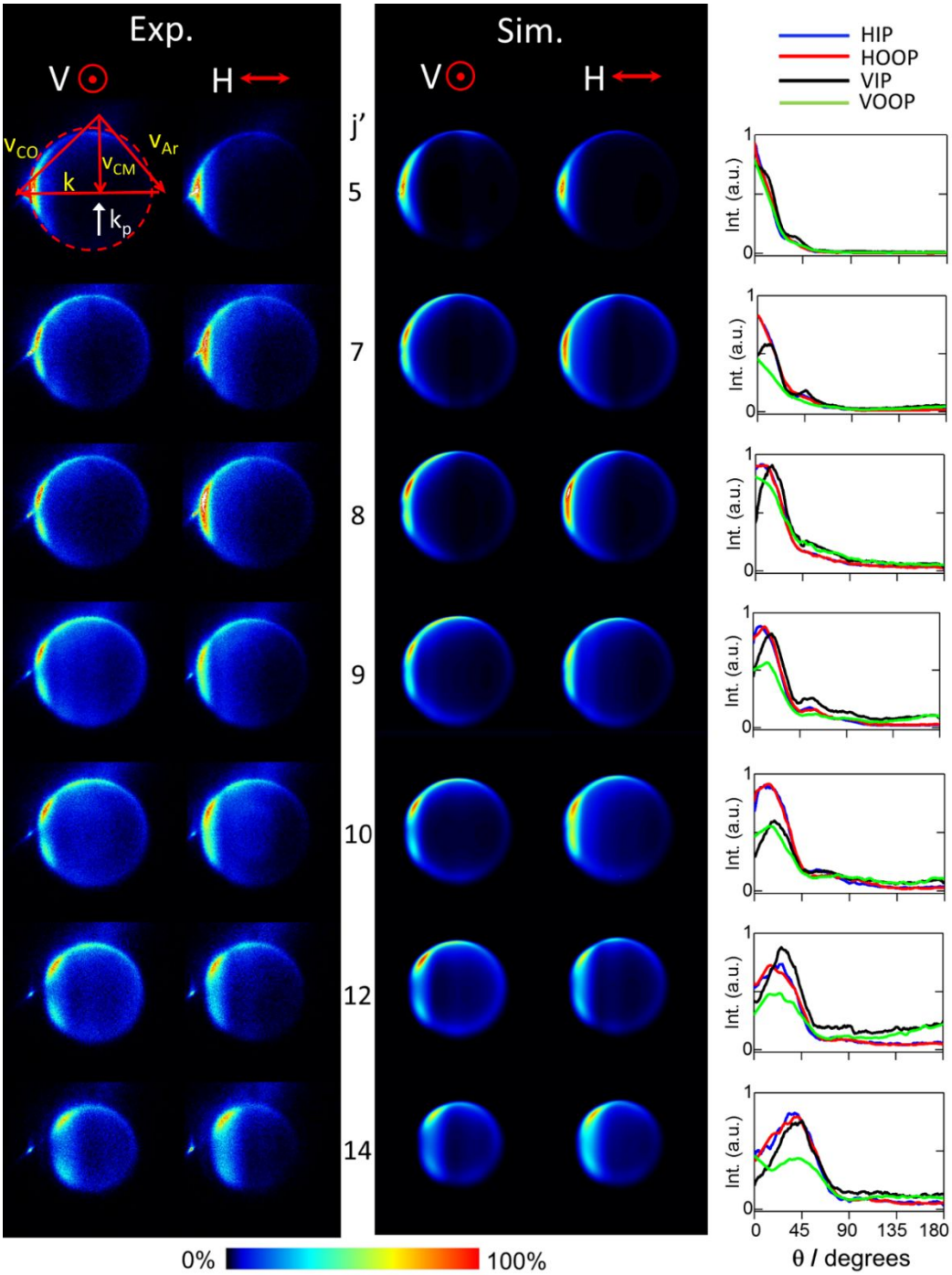

Figure 5: The left and middle columns show Experimental (Exp.) and simulated (Sim.) scattering images of CO+Ar system obtained with Horizontal (H) and Vertical (V) polarization of VUV light for final rotational states in the range of j' = 5 - 14 at collision energy 700 cm^{-1}. Images are presented such that the relative velocity vector is directed horizontally with forward scattering region positioned on the left side of the image. The Newton diagram for the collision is overlaid on the V experimental image for the product state j' = 5, where arrows indicate the velocity vectors of colliders: $\mathbf{v}_{CO}$ and $\mathbf{v}_{Ar}$, the center of mass velocity $\mathbf{v}_{CM}$, the initial relative velocity vector $\mathbf{k}$, and the probe laser beam propagation direction $\mathbf{k}_p$, while the ring represents the CO scattered plane on the detector. Angular distribution components HIP, HOOP, VIP and VOOP extracted from these experimental H and V images are shown in

the right column.

The resulting polarization-free differential cross sections (conventional DCSs) and polarization-dependent differential cross sections (alignment moments in the current case) derived from analysis of the HIP, HOOP, VIP, and VOOP curves, in comparison with theory are shown in Figure 6 and Figure 7, respectively. The experimental DCSs are compared with the collision energy averaged CC QM calculations on the potential surface of Pedersen *et al*. (ref. 32), as well as with the QCT calculations on the recalculated CCSD(T)-AVQZ potential surface. Because of the difficulty of determining the absolute cross sections in VMI experiments, only relative state-to-state DCSs are available. Therefore, the experimental DCSs have been area normalized to the CC QM calculation results, excluding regions with large deviations between experiment and CC QM predictions (namely the very forward region) for all states, in order to offer a good visualization for comparison. We noted that for the QCT calculations, no DCSs are available for the *j*' = 12 and *j*' = 14 states in the classically forbidden regions at low scattering angle.

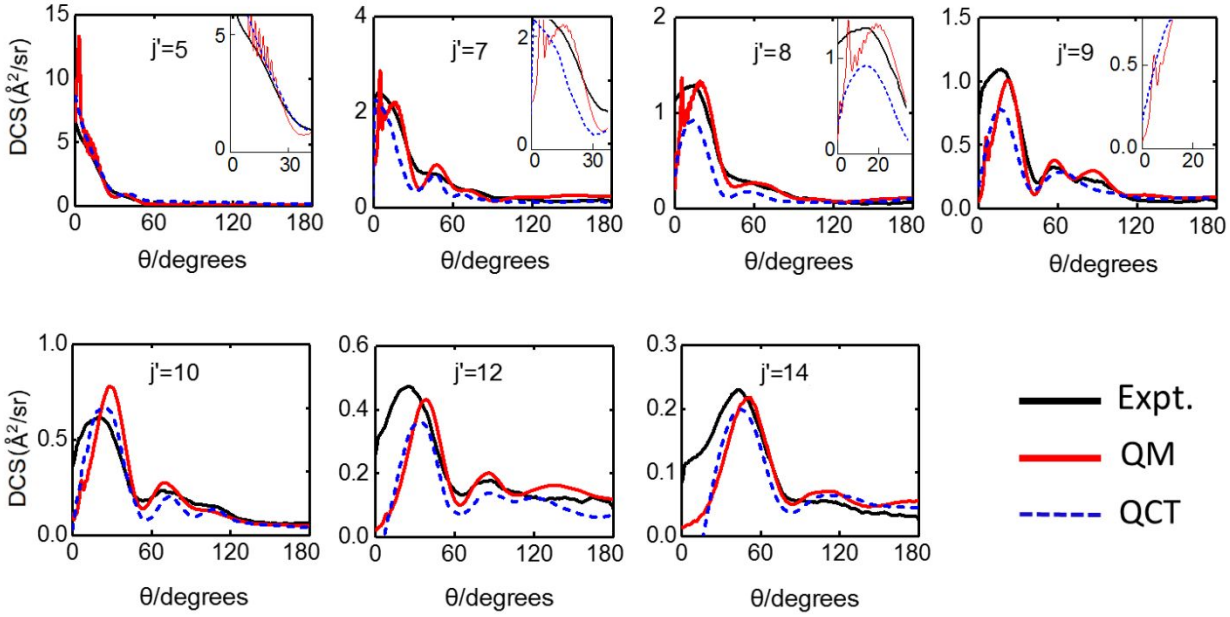

Figure 6: Comparison of the experimental (black solid line), CC QM calculated (red solid line) and QCT calculated (blue dashed line) polarization-free differential cross sections (i.e., conventional DCSs) for the scattered CO final rotational states *j*'= 5, 7, 8, 9, 10, 12 and 14 at a mean collision energy of 700 cm^{-1}. The experimental alignment-free DCSs were obtained from analysis of HIP, HOOP, VIP, and VOOP curves extracted from the experimental images with H & V polarization. In order to visualize a good comparison between experiment and theory, the experimental results are normalized to the QM predicted data by making the area integration of $\int \mathrm{DCS}(\theta)\sin\theta d\theta$ from the experimental DCS equal to that from the QM predicted DCS. Inserts on the top row show expanded views of the near-forward scattering range to show the oscillations in CC QM predicted DCSs for *j*' = 5,7,8,9 states.

Overall, the majority of the experimentally measured behavior in DCSs, such as the number, location, and intensity of the maxima, generally agrees well with the theoretical results predicted by both CC QM and QCT calculations, in spite of a few perceptible intensity differences of the

DCS valleys between maxima on closer inspection of Figure 6. The most obvious deviations between experiment and theory appear in the very forward scattering angle region below 15°, where the experimental DCSs have more significant intensity than theory predictions from both sets of calculations, for most of the *j*' states. The inserts on the top row of Figure 6, in an expanded view, show the oscillations of DCSs in the near-forward scattering range for *j*' = 5, 7, 8, 9 states predicted by CC QM calculations. The rapid oscillations mainly in the 0°-20° range, which are attributed to diffraction oscillations by QM theory, are not resolved in the experiment owing to its limited angular resolution. The discrepancy or the mismatch of DCSs between theory and experiment in forward scattering especially for higher final states can result from many factors. One of the key factors is the presence of elastic scattering of which the DCS is strongly distributed in forward scattering regime with the collision cross section being very high relative to the inelastic scattering. The presence of higher states in the parent beam can also lead to a higher apparent cross section, as shown in ref. 23.

Turning to the rank 2 renormalized PDDCSs, *i.e.*, the alignment moments, Figure 7 shows the experimental $A_0^{\{2\}}(\theta)$ and $A_{2+}^{\{2\}}(\theta)$ moments together with theoretical predictions using CC QM calculations, QCT calculations and the kinematic apse (KA) model. For the $A_0^{\{2\}}(\theta)$ moments in the left panel, we first notice the generally quite good agreement between the measurements and the CC QM, and QCT results over all the final states. Overall, the $A_0^{\{2\}}(\theta)$ moments range from positive values in the forward direction to extreme negative values in the backward direction, indicating that a 'propeller'-like rotation motion is mostly dominating the forward direction while a 'Frisbee'-like motion dominates in the backward scattering region. This trend is similar to the observations from the work of Brouard *et al*. on NO+Ar collisions.[21] However, careful comparison between the experiment, CC QM calculations and QCT calculations reveals that the experimental $A_0^{\{2\}}(\theta)$ moments have some deviations in the forward scattering region (θ < 20°); this could be attributed to the presence of elastic scattering as the collision induced alignment effect due to elastic scattering and inelastic scattering are opposite in nature.[23] On closer inspection, QCT-predicted $A_0^{\{2\}}(\theta)$ moments follow surprisingly closely the CC-QM calculations, though the very rapid oscillations of CC-QM moments at small scattering angles due to quantum interferences are not predicted by QCT calculations.

Relatively broad structures in the forward and sideways region (θ < 90°) can be seen in both CC-QM predicted and QCT-predicted moments as a function of scattering angle for all final *j*' states. The location of the structures moves to larger scattering angles as *j*' increases, indicating that QCT calculations not only do a good job in predicting DCSs but also alignment moments. In contrast to CC QM and QCT results, the $A_0^{\{2\}}(\theta)$ moments predicted by the KA model display very smooth shapes over all scattering angles. In addition, despite good agreement in the backward scattering region which is dominated by the repulsive part of the interaction potential, the KA model predictions deviate significantly from the experimental results, as well as from the results of the CC QM and QCT calculations in the forward scattering region, where the attractive character also plays a role. These observations imply that the alignment moments in the inelastic

scattering of CO+Ar at a collision energy of 700 cm^{-1} are not well described by KA model.

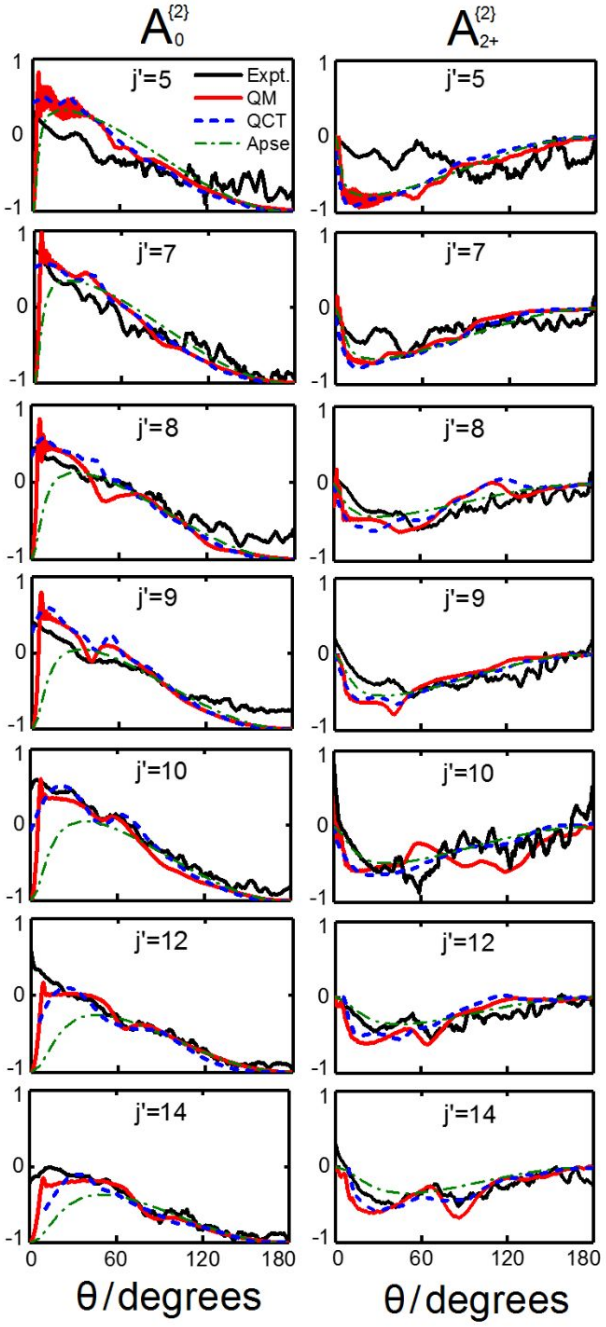

Figure 7: Experimental $A_0^{\{2\}}(\theta)$ (left panel) and $A_{2+}^{\{2\}}(\theta)$ (right panel) rank 2 renormalized PDDCSs in comparison with theory for the scattered CO final rotational states *j'* = 5, 7, 8, 9, 10, 12 and 14 at a mean collision energy of 700 cm^{-1}. The experimental (black solid line) alignment moments $A_0^{\{2\}}(\theta)$ and $A_{2+}^{\{2\}}(\theta)$ were obtained from analysis of HIP, HOOP, VIP, and VOOP curves extracted from the experimental H & V images. The theoretical predictions were calculated using different methods: CC QM calculations (red solid line), QCT calculations (blue dashed line) and kinematic apse model calculations (dark green dash-dotted line).

Finally we can see that all the $A_0^{\{2\}}(\theta)$ moments, both experiment and theory predictions, shift downwards across the entire range of scattering angles as *j*' increases. This is reasonable because the scattering becomes more and more impulsive when the degree of rotational excitation increases, and the classical hard-shell nature of the interaction increasingly dominates the dynamics responsible for collision induced alignment.

The experimental $A_{2+}^{\{2\}}(\theta)$ moments in comparison with different theoretical predictions are shown in the right panel of Figure 7. As is typical, the $A_{2+}^{\{2\}}(\theta)$ moments are not as reliable as the $A_0^{\{2\}}(\theta)$ moments because in the case of the direct extraction method not all the angular distribution components are used to extract the rank 2 component 2+ polarization moments.[23, 24] Though the experimental $A_{2+}^{\{2\}}(\theta)$ moment results are noisy, they capture the essence of the CC QM and QCT predictions, including the overall magnitude, the overall shape and some interesting structures in the most forward scattering region, for all the product states except *j*' = 5. The significant discrepancy of $A_{2+}^{\{2\}}(\theta)$ moments between experiment and theory particularly in the forward hemisphere for the *j*' = 5 state is mainly caused by the overlap of the molecular beamspot with the scattering Newton sphere on the image, which introduces a strong depolarization effect by elastic scattering to the forward scattering parts, as also shown in the graph for $A_0^{\{2\}}(\theta)$ moments of the same final state in Figure 7. Another perceptible disagreement between experimental results and theoretical predictions occurs at $\theta \approx 60°$ in the $A_{2+}^{\{2\}}(\theta)$ graph for *j*' = 10, where a dip (minimum) is observed experimentally while the CC QM calculation predicts a bump and the QCT and KA predictions are smooth. The origin of the differences between various calculations are not clear yet; however the behavior of the measurements could originate from the detection bias caused by the partial overlap between the probed Q(10) line and the nearby perturbative state as shown in Figure 2. Again, good agreement regarding the relative strength, shape and structures can generally be seen when the QCT-predicted $A_{2+}^{\{2\}}(\theta)$ moments are compared to experimental and CC QM results, offering support for the reliability of QCT calculations for CO scattering studies. It is perhaps not surprising that within the measurable range, *i.e.*, the classically allowed region, the experimentally observed behavior is again not predicted well by the KA model, reflecting the fact that the intermolecular interaction between CO and Ar for the collision cannot be characterized as purely repulsive.

Considering the amplitude of $A_0^{\{2\}}(\theta)$ and $A_{2+}^{\{2\}}(\theta)$ moments, both the two theoretical predicted alignment moments possess larger absolute values of their extrema in amplitude than the predictions in previous theoretical studies on rotational alignment in NO-rare gas inelastic scattering. And, similar to the collision induced alignment study of CO+He,[23] both the two experimental alignment moments in this work tend to reach their extrema values which are predicted by theory, whereas in the previous studies on scattering of NO with rare gases,[18, 19, 21] the corresponding extrema values were not reached experimentally. For instance, the $A_0^{\{2\}}(\theta)$ moment in the NO+Ar rotational alignment study[21] typically reaches only around -0.5 instead of the theoretically predicted minimum value of -1 at the backward scattered angles. In other

words, collision experiments reveal less alignment for scattered NO products than for CO products. The difference in degree of alignment between NO and CO can arise for several reasons. Unlike the CO molecule, NO possesses a nuclear spin I = 1, which can couple to the electronic angular momentum via stray magnetic fields, leading generally to a depolarization of the rotational alignment of the nascent NO on the time scale of scattering experiment. This effect is called "hyperfine coupling depolarization" and has been discussed extensively in the past.[40-42]

5 Conclusion and Outlook

We have studied the stereodynamics of CO+Ar inelastic scattering at a mean collision energy of 700 cm^{-1} using VUV REMPI detection. We have reported experimental measurements of the state-to-state DCSs and scattering angle-dependent rotational angular momentum alignment moments for CO products scattered into a range of final *j*' states. This shows that our analysis method for extraction of polarization dependent differential cross sections (PDDCSs) directly from the experimental data works quite well for CO+Ar collisions. The obtained DCSs and alignment moments display very good agreement with theory predictions by CC QM and QCT calculations. While the rapid diffraction oscillation structures due to quantum mechanical interference in the forward scattering region cannot be predicted by QCT calculations, the QCT predicted results of DCSs and alignment moments closely follow those from CC QM predictions; both sets of calculations well reproduce the features observed in measurements including the shapes, peak locations and amplitude. These indicate the good accuracy of the potentials within the energy region sampled in this experiment and the reliability of QCT calculations for stereodynamics of inelastic scattering involving CO for the studied collision energy. In another test, QCT calculations for CO+He inelastic scattering at a collision energy of $\sim$ 840 cm^{-1} were performed as well and the results were compared with the experimental measurements using our VUV REMPI detection scheme, and with the corresponding CC QM calculations[23]. Very good agreement between QCT and CC QM predictions was found again, and both of them agree with the experiment.

In general, the observed trends of $A_0^{\{2\}}(\theta)$ moments for CO+Ar are quite similar to those reported for the NO+Ar system[21], and are in quantitative agreement with the intuitive predictions of "propeller" versus 'frisbee' motion provided by the classical kinetic apse (KA) model. However, a substantial discrepancy can be seen between the KA model predictions and the experimental, CC QM, and QCT predictions for all the final states, implying that the intermolecular interaction between CO and Ar cannot be characterized as purely repulsive for these collisions.

The experimental CO+Ar PDDCSs are more reliable than those from the previous CO+He study[23], which reflects the larger cross sections and more favorable kinematics for Ar compared to He scattering. The direct analysis method relies on integration along a stripe through the plane of the 2-D crushed image and thus partial slicing should be avoided. This is possible for inelastic scattering images which (even for CO+Ar) are still relatively small. We are currently testing a direct analysis adapted for partial slicing using CO images from the photodissociation of OCS and CO_2 around 154 nm using our VUV REMPI detection method.

ACKNOWLEDGEMENTS

DHP, ZFS, LS, and AvdA acknowledge the NWO-Dutch Astrochemistry Network II project number 648.000.024, and the NWO-TOP project number 715.013.002 for support. AGS gratefully acknowledges the Radboud Excellence Initiative and support from the National Science Foundation under award number CHE-1634760. All the authors thank M. Brouard for helpful discussions and for making available a program that allows the calculations of the alignment moments based on the kinematic apse model which was coded by B. Hornung.

REFERENCES

1. A. von Zastrow, J. Onvlee, S. N. Vogels, G. C. Groenenboom, A. van der Avoird and S. Y. T. van de Meerakker, *Nat. Chem.*, 2014, **6**, 216-221.
2. M. Brouard and C. Vallance, *Tutorials in Molecular Reaction Dynamics*, The Royal Society of Chemistry, UK, 2012.
3. J. J. Gilijamse, S. Hoekstra, S. Y. T. van de Meerakker, G. C. Groenenboom and G. Meijer, *Science*, 2006, **313**, 1617-1620.
4. K. T. Lorenz, D. W. Chandler and G. C. McBane, *J. Phys. Chem. A*, 2002, **106**, 1144-1151.
5. S. Antonova, A. Lin, A. P. Tsakotellis and G. C. McBane, *J. Chem. Phys.*, 1999, **110**, 2384-2390.
6. S. Antonova, A. Lin, A. P. Tsakotellis and G. C. McBane, *J. Chem. Phys.*, 1999, **110**, 11742-11748.
7. L. S. Bontuyan, A. G. Suits, P. L. Houston and B. J. Whitaker, *J. Chem. Phys.*, 1993, **97**, 6342-6350.
8. A. G. Suits, L. S. Bontuyan, P. L. Houston and B. J. Whitaker, *J. Chem. Phys.*, 1992, **96**, 8618-8620.
9. H. Meyer, *J. Phys. Chem.*, 1995, **99**, 1101-1114.
10. H. Meyer, *Chem. Phys. Lett.*, 1994, **230**, 519-524.
11. A. T. J. B. Eppink and D. H. Parker, *Rev. Sci. Instrum.*, 1997, **68**, 3477-3484.
12. M. P. de Miranda, F. J. Aoiz, L. Banares and V. S. Rábanos, *J. Chem. Phys.*, 1999, **111**, 5368-5383.
13. F. J. Aoiz, M. Brouard and P. A. Enriquez, *J. Chem. Phys.*, 1996, **105**, 4964-4982.
14. E. A. Wade, K. T. Lorenz, D. W. Chandler, J. W. Barr, G. L. Barnes and J. I. Cline, *Chem. Phys.*, 2004, **301**, 261-272.
15. J. I. Cline, K. T. Lorenz, E. A. Wade, J. W. Barr and D. W. Chandler, *J. Chem. Phys.*, 2001, **115**, 6277-

6280.
16. K. T. Lorenz, D. W. Chandler, J. W. Barr, W. W. Chen, G. L. Barnes and J. I. Cline, *Science*, 2001, **293**, 2063-2066.
17. M. Brouard, H. Chadwick, S. D. S. Gordon, B. Hornung, B. Nichols, F. J. Aoiz and S. Stolte, *J. Phys. Chem. A*, 2015, **119**, 12404-12416.
18. H. Chadwick, B. Nichols, S. D. S. Gordon, B. Hornung, E. Squires, M. Brouard, J. Kłos, M. H. Alexander, F. J. Aoiz and S. Stolte, *J. Phys. Chem. Lett.*, 2014, **5**, 3296-3301.
19. M. Brouard, H. Chadwick, S. D. S. Gordon, B. Hornung, B. Nichols, J. Kłos, F. J. Aoiz and S. Stolte, *J. Chem. Phys.*, 2014, **141**, 164306.
20. M. Brouard, B. Hornung and F. J. Aoiz, *Phys. Rev. Lett.*, 2013, **111**, 183202.
21. M. Brouard, H. Chadwick, C. J. Eyles, B. Hornung, B. Nichols, F. J. Aoiz, P. G. Jambrina and S. Stolte, *J. Chem. Phys.*, 2013, **138**, 104310.
22. Z. F. Sun, A. D. von Zastrow and D. H. Parker, *J. Chem. Phys.*, 2017, **147**, 013909.
23. L. Song, G. C. Groenenboom, A. van der Avoird, C. K. Bishwakarma, G. Sarma, D. H. Parker and A. G. Suits, *J. Phys. Chem. A*, 2015, **119**, 12526-12537.
24. A. G. Suits, C. K. Bishwakarma, L. Song, G. C. Groenenboom, A. van der Avoird and D. H. Parker, *J. Phys. Chem. A*, 2015, **119**, 5925-5931.
25. A. J. Orr-Ewing and R. N. Zare, *Annu. Rev. Phys. Chem.*, 1994, **45**, 315-366.
26. B. Yan, P. F. H. Claus, B. G. M. van Oorschot, L. Gerritsen, A. T. J. B. Eppink, S. Y. T. van de Meerakker and D. H. Parker, *Rev. Sci. Instrum.*, 2013, **84**, 023102.
27. R. Hilbig and R. Wallenstein, *Appl. Opt.*, 1982, **21**, 913-917.
28. S. -M. Wu, X.-M. Yang and D. H. Parker, *Mol. Phys.*, 2005, **103**, 1797-1807.
29. C. M. Western, *PGOPHER*, *a Program for Simulating Rotational, Vibrational and Electronic Structure*, version 8.0, University of Bristol, 2014, http://pgopher.chm.bris.ac.uk.
30. M. Brouard, H. Chadwick, C. J. Eyles, B. Hornung, B. Nichols, F. J. Aoiz, P. G. Jambrina, S. Stolte and M. P. de Miranda, *J. Chem. Phys.*, 2013, **138**, 104309.
31. G. C. McBane, *Imsim*, a *program for simulating images from crossed-beam scattering experiments with laser photoionization and 2D velocity mapping detection,* version 3.0, 2018, http://faculty.gvsu.edu/mcbaneg/.
32. T. B. Pedersen, J. L. Cacheiro, B. Fernandez and H. Koch, *J. Chem. Phys.*, 2002, **117**, 6562-6572.
33. M. H. Alexander, *Faraday Discuss.*, 1999, **113**, 437-454.
34. M. H. Alexander, *J. Chem. Phys.*, 1977, **67**, 2703-2712.
35. A. J. C. Varandas, *Chem. Phys. Lett.*, 1994, **225**, 18-27.
36. H.-J. Werner, P. J. Knowles, G. Knizia, F. R. Manby and M. Schütz, *Comput. Mol. Sci.*, 2012, **2**, 242-253.
37. X. Hu, W. L. Hase and T. Pirraglia, *J. Comput. Chem.,* 1991, **12**, 1014-1024.
38. J. A. Coxon and P. G. Hajigeorgiou, *J. Chem. Phys.,* 2004, **121**, 2992-3008.
39. V. Khare, D. J. Kouri and D. K. Hoffman, *J. Chem. Phys.*, 1981, **74**, 2275-2286.
40. M. Rutkowski and H. Zacharias, *Chem. Phys.*, 2004, **301**, 189-196.
41. A. J. Orr-Ewing, W. R. Simpson, T. P. Rakitzis and R. N. Zare, *Isr. J..Chem.*, 1994, **34**, 95-102.
42. R. Altkorn, R. N. Zare and C. H. Greene, *Mol. Phys.*, 1985, **55**, 1-9.